

Modifying and Fine Controlling of Silver Nanoparticle Nucleation Sites and SERS Performance by Double Silicon Etching Process

Allaa A. Jabbar¹ · Alwan M. Alwan¹ · Adawiya J. Haider¹

Received: 26 January 2017 / Accepted: 9 May 2017 / Published online: 16 June 2017
© Springer Science+Business Media New York 2017

Abstract Different forms of modified and well-controlled plasmonic silver nanoparticles (AgNPs) were synthesized by silver ion reduction process of porous silicon (PS). Fine control of PS surface morphology was accomplished by employing two etching processes: light-induced etching (LIE) and photo electrochemical etching (PECE). The idea was to prepare excellent and reproducible surface-enhanced Raman scattering (SERS) substrates with high enhancement performance. PS surface modification was employed to create efficient and nearly uniformly distributed AgNP hotspot regions with very high specific surface areas. Reproducibility deviation of no more than 5% and enhancement factor of 1.2×10^{14} were obtained by SERS measurements at very low, rhodamine 6G (R6G) dye, concentration 10^{-15} M. The PS morphology SERS substrate was well discussed and analyzed using field emission scanning electron microscopy (FE-SEM), X-ray diffraction spectroscopy (XRD), and Raman measurements.

Keywords Porous silicon · Double etching processes · Hotspots · Surface-enhanced Raman scattering · Reproducibility · Single molecule detection

Introduction

Surface-enhanced Raman scattering (SERS) has become widely recognized as a powerful tool to investigate several

applications, specially the food quality fields [1]. In Raman scattering applications, SERS effect consists of vibrational modes, originating from species adsorbed on or in the vicinity of nanostructured materials [2]. SERS has become the most studied Raman-based technique for analytical purposes [3]. Improving the SERS efficiency through maximizing the hotspot density with specific nanoparticle sizes, excellent uniformity, and reproducibility together with an easy and low-cost fabrication are the main targets of quantitative analysis [4]. Porous silicon is an extremely versatile material due to its excellent electrical, optical, morphological, and chemical properties, which can be modified according to the etching process [5]. Different etching processes, such as laser-induced etching (LIE) and photo electrochemical etching (PECE), are employed to synthesize n-type silicon porous layer. LIE of silicon is a relatively infrequent technique for creating silicon nanostructures [6], where electron hole pairs are generated, after absorbing incident laser photons, in a localized area. Controlling the surface morphology of the LIE porous structure is of great interest since the surface area of the porous layer would determine the field of application [7, 8]. In PECE, an external current is employed in addition to photon excitation. This type of etching is commonly performed within an electrochemical cell on n-type silicon since photo-excitation is required to make free carriers available for conduction at low voltages [9–11]. Previous work has demonstrated large specific area and governable nano-porous silicon structure can increase the amount of effective hotspots and enhance the sensitivity of the SERS signals. Compared to well-known electroless [12], electrochemical [13], and metal-assisted wet etching [14] porous silicon production methods, SERS-active layer is usually deposited by thermal decomposition [15], immersion plating [16, 17], and physical vapor deposition (PVD) [18]. In the current work, coarse and fine modification of the porous silicon (PS) morphology has

✉ Allaa A. Jabbar
allaabaldawi2015@gmail.com

¹ Department of Applied Sciences, University of Technology, Baghdad, Iraq

been conveyed by double etching process of silicon to synthesis specific, efficient, and multi-plasmonic Ag NP hybrid structures. SERS performance parameters (analytic enhancement factor and reproducibility) have been investigated and analyzed.

Experimental Part

Chemical Materials

As received, hydrofluoric acid 48% (Merck Life Science—India) was diluted with absolute ethanol 99.8% (Sigma-Aldrich—Germany) to form 24% HF etching concentrations. Silver nitrite (AgNO_3) (99.9%) was dissolved in deionized water to prepare 0.01 M solution, and finally rhodamine 6G (R6G) dye was utilized to confirm the SERS efficiency.

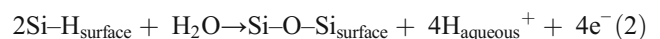
Porous Silicon Fabrication

PS layers were fabricated by two etching techniques: LIE and PECE with short CW diode laser wavelength 405 nm at 20 mW/cm^2 laser intensity (class IIIb laser product). Phosphorus-doped n-type (100)-oriented silicon substrate of $10 \Omega \text{ cm}$ resistivity and $500 \mu\text{m}$ thickness was etched. In the LIE, 1 cm^2 area of the silicon surface was illuminated by the laser radiation for 10 min etching time, followed by PECE process in a Teflon cell equipped with two platinum electrodes as cathode and silicon sample as anode and the distance between platinum ring and silicon wafer was 1 cm. Different PS samples were prepared at various etching times (5, 10, 15, and 20 min) and constant (10 mA/cm^2) current density. The etching electrolyte solution was 1:1, 48% hydrofluoric acid:98% ethanol, by volume. The etching techniques are illustrated in Fig. 1.

Preparation of Hybrid Structures (Silver Nanoparticles/Porous Silicon)

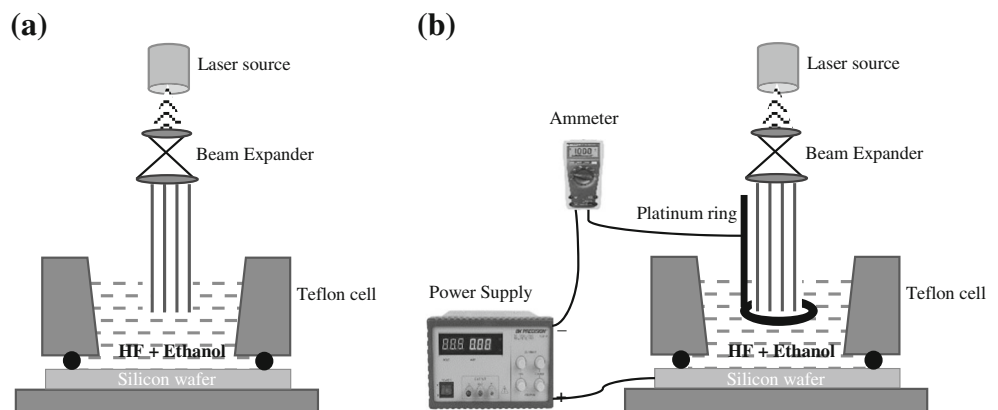
Hybrid structures (AgNPs/PS) were prepared by LIE and PECE processes, after immersing bare PS substrates in aqueous solution of AgNO_3 for 15 min. Sample 1 refers to the hybrid structure AgNPs/PS, in which the PS layer was prepared by LIE process only. Samples 2, 3, 4, and 5 refer to hybrid structures AgNPs/PS, in which the PS layers were prepared by LIE followed by PECE at 5, 10, 15, and 20 min, respectively. The AgNO_3 solution concentration was of 10^{-2} M and the dipping process was performed at room temperature.

In silver immersion plating, the formation of AgNPs on porous surfaces takes place via the Volmer-Weber growth mechanism [13]. When the porous silicon substrate was put in the AgNO_3 solution, silver reduction process will occur according to these equations [19]:



Due to these reactions, silver nuclei will be formed at the boundaries of pores, hence filling the porous silicon surface gradually by aggregated island of silver. Immersion deposition process is affected by many important parameters of solution condition and the surface state of the substrate such as the morphology of porous silicon which supplied a high density of suitable sites for growth and nucleation of Ag nanocrystals, so the number of Si-H bonds is very important for silver reduction process through immersion of porous silicon into AgNO_3 solution. Metal ion concentration and the duration of immersion process also affect the metal growth process [19].

Fig. 1 Schematic diagram of etching processes. **a** LIE process. **b** PECE process



Characterizations

The morphological properties of PS and AgNPs/PS surface morphology characteristics were studied in this work using Zeiss ULTRA-55 FEG scanning electron microscopy with resolution 1 nm. The photoluminescence spectrum of the AgNPs/PS samples was measured by utilizing CW 325 nm, 400 mW He-Cd laser. The photoluminescence (PL) system is based around a Horiba Jobin-Yvon T64000 spectrometer system. Raman spectra of trapped molecules within as-prepared PS and AgNPs/PS hybrid samples were done by a micro Raman spectrometer (1000 B) with (detector imaging: CCD), (excitation laser Ar-514 nm), (grating 1800 line), (accumulation 1), (power 10 mW), 60 s time.

Results and Discussions

Porous Silicon Characterization

Figures 2 and 3 portray the variations of PS surface prepared by means of two etching techniques.

Figures 2 and 3 portray the variations of PS surface prepared by means of two etching techniques: LIE and PECE. Dramatic changes of the PS surface morphology were observed due to the double etching process. In the LIE process, the FE-SEM images of PS conveyed a PS surface containing a network of random distributed, non-connected, and early formed 10–40-nm pores with different sizes and shapes. Figure 3a–d presents FE-SEM images of LIE-fabricated PS layers, followed by PECE using 10 mA/cm² etching current density at 5, 10, 15, and 20 min etching times. This was done to modify the overall PS morphology, where two types of morphology were distinguished. At 5 and 10 min etching times, the PS surface is characterized with pore-like square pores. The square pores’ dimensions and density increased with time and an overlapping process of pores has resulted

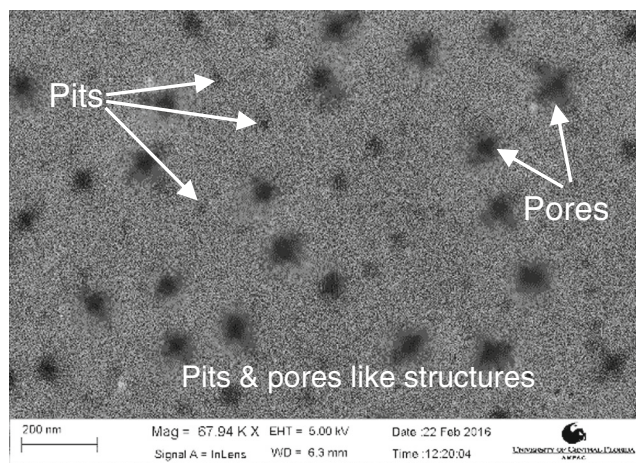


Fig. 2 FE-SEM images of PS prepared by LIE process

at 10 min etching time. Comparing with Fig. 2, these changes in the PS morphology are related to the external current, which enhanced the silicon dissolution process of the LIE—early formed pores—and helped the formation of complete pores. The pore sizes were increased when increasing the etching time from 5 to 10 min. The PECE process to higher etching times (15 and 20 min) has transferred the pore morphology to a new infrequent cross-like structure (quad-star pores) with different sizes [20]. Figure 3c illustrates incompletely connected pores along the cross axis. The density of these cross-like pores is not very large compared to that of the non-etched silicon regions. Further increase of etching time to 20 min helped connecting the branches of adjacent pores as shown in Fig. 3d. The visual diagnostics of the pores’ shape reflect a gradient behavior in the porous sizes, where the pores extended vertically across the silicon regions with decreasing sizes. The double etching process has modified the overall PS morphology to an extent related to the etching time as shown in the sequence surface morphologies in Fig. 4.

This anisotropic etching would alter the inhomogeneity of the porous surface and hence enlarge the density of the dangling bonds localized at the porous surface. The finger print of these bonds was clear in the natures of the resulting silver nanoparticle layer deposited over the PS surface. The PL spectra of the bare PS samples for different etching processes are illustrated in Fig. 5. For sample 1, the peak of PL spectra is located at 701 nm with 1099 au. The role of PECE process on the PL spectra is clearly observed on both the peak and the intensity of the PL curves.

The effect of increasing the etching time during PECE process has led to an increase in the PL with a blue shift of the PL peak position. Table 1 lists the average values of silicon nano-walls (*d*) resulted from PECE for different etching times of the LIE process. The average silicon nano-size (*d*) was calculated from Eq. 4 [21]:

$$E_{(eV)} = E_g + \frac{h^2}{8d^2} \left[\frac{1}{m_e^*} + \frac{1}{m_h^*} \right] \tag{4}$$

where $E_{(eV)}$ is the PL peak position of PSi, $E_g = 1.12$ eV is the energy band gap of bulk Si, $h = 4.13 \times 10^{-15}$ eV s is Planck’s constant, $m_e^* = 0.19 m_0$, $m_h^* = 0.16 m_0$, and $m_0 = 9.1 \times 10^{-31}$ kg [21].

In Table 1, the PS prepared by the LIE process alone (sample 1) showed the lowest value of energy gap $E_g = 1.77$ eV and the greatest value of nano-wall size $d = 6.45$ nm. For the PS prepared via double etching process, samples 2, 3, 4, and 5, the E_g increased from 1.82 to 2.14 eV and the nano-sizes (*d*) decreased from 6.29 to 5.13 nm when increasing the etching time from 5 to 20 min. These variations in the PS properties are related to the dynamic behavior of the silicon dissolution rate during the etching sequence, where the resulting of entire

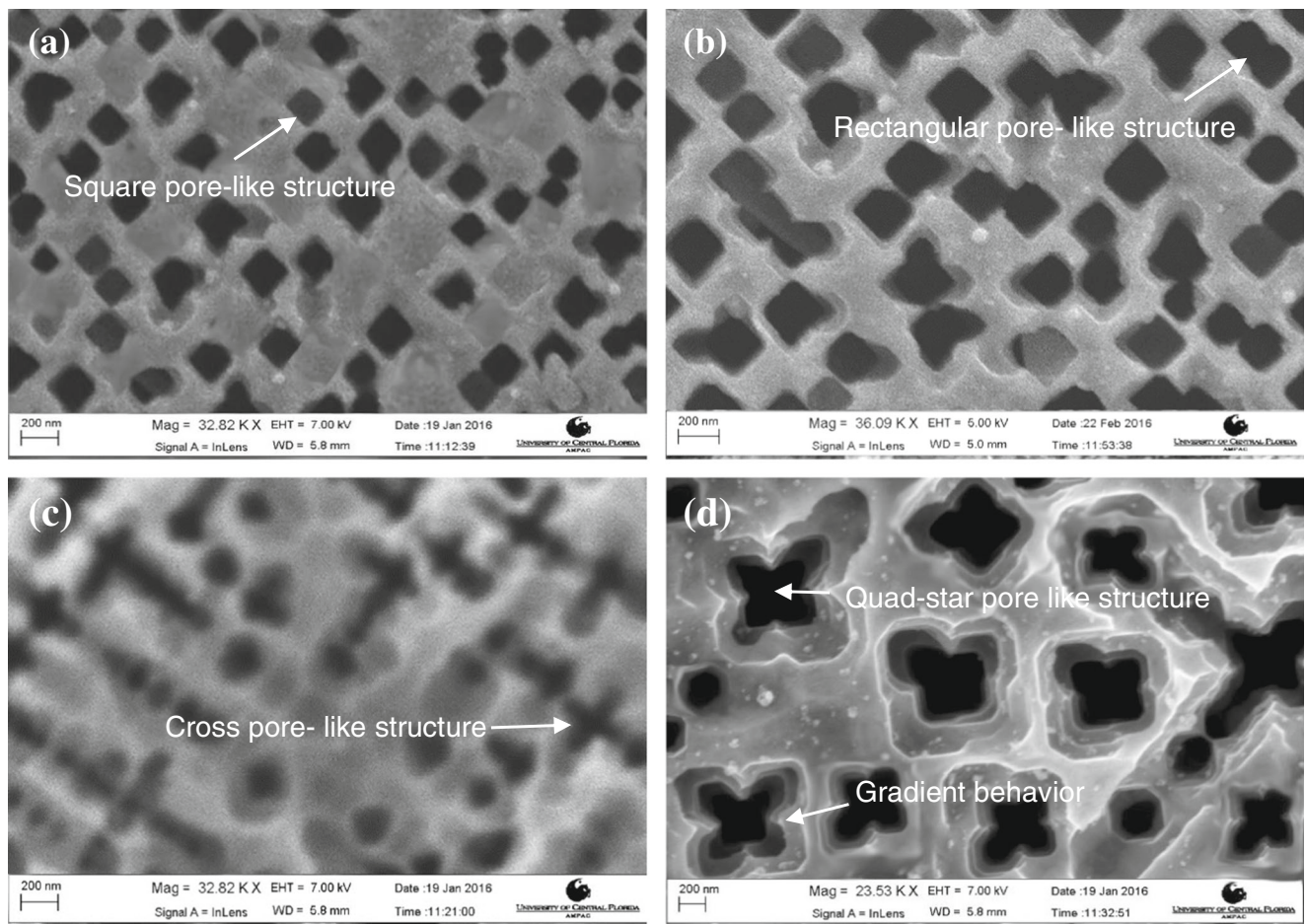


Fig. 3 FE-SEM images of porous silicon samples prepared by LIE process followed by PECE process with etching current density 10 mA/cm² and etching times of **a** 5 min, **b** 10 min, **c** 15 min, and **d** 20 min

photocurrent density J_{ph} is generated due to the absorption of the incident photon as given in Eq. 5 [21]:

$$J_{ph} = \frac{P(1-R)\eta}{h\nu A} \times q \tag{5}$$

where P is the incident laser intensity, R is a reflectivity of PS surface, η is a quantum efficiency, ν is a laser frequency, A is the PS area ($\approx 1 \text{ cm}^2$), h is Planck's constant $6.6 \times 10^{-34} \text{ J s}$, and q is the electric charge $1.6 \times 10^{-19} \text{ C}$ [21]. This lower value of current density would initiate the etching process at low etching rate so that the density of replacing Si–Si bonds

with Si–F bonds is small. This has resulted in an incomplete silicon surface coverage, leaving large number of pits or the pores under formation process. The external current ($J_{external}$) used was generated from applying external fixed voltage of about 5 V. $J_{external}$ was controlled by Ohm's law as:

$$J_{external} = V_{external} / \rho L \tag{6}$$

where ρ is a resistivity of PS and σ is the conductivity of PS, given as $\sigma = 1/\rho$, so:

$$J_{external} = V_{external} (\sigma / L) \tag{7}$$

Fig. 4 Schematic of pore shaping sequence

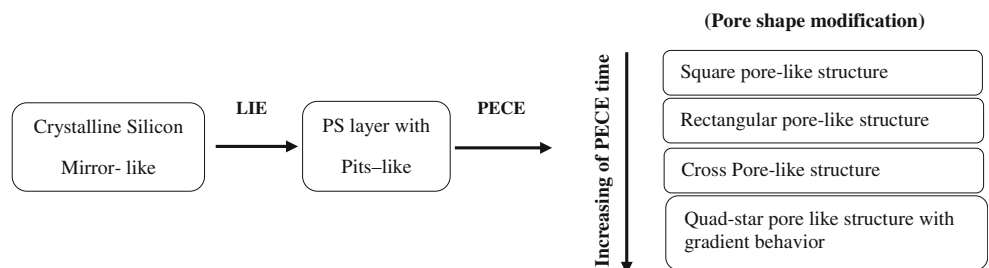
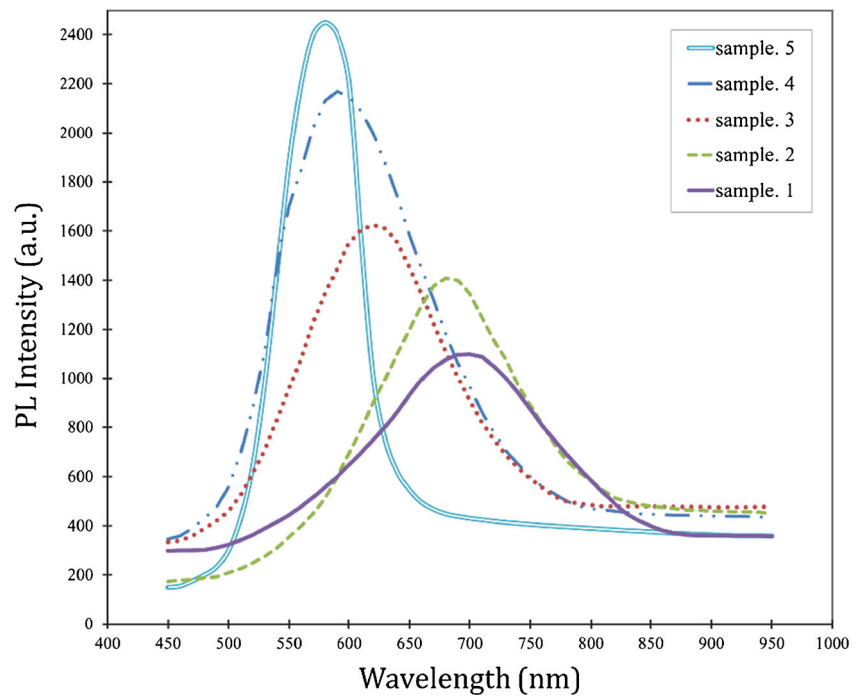


Fig. 5 Photoluminescence spectra of PS samples



The PS conductivity is a porosity-limited process during the etching cycle [22], and according to the M. ben-Chorin et al. [23] model, the conductance of PS layer and hence the current passing through is varied with the applied voltage (V), activation energy (E_a), and PS layer parameters like porous thickness (L) and embedding (ϵ_r) medium in exponential form as shown in Eq. 8:

$$G_{(V,T)} = G^0 \exp\left[-\frac{E_a}{KT}\right] \exp\sqrt{V/V^*} \tag{8}$$

where the value of V^* is given by [24]:

$$\sqrt{V^*} = \frac{KT}{q} \left[\frac{q}{\pi \epsilon \epsilon_r h} \right]^{-1/2} \tag{9}$$

The value of dielectric constant ϵ_r is a function of the porosity of PS layer (P) according to reference [24]:

$$\epsilon_{r_{ps}} = \epsilon_{r_{si}} - P(\epsilon_{r_{si}} - \epsilon_{r_{pore}}) \tag{10}$$

So:

$$J_{total} = J_{external} + J_{internal} \tag{11}$$

To a large extent, the increase of porosity would prevent the absorption of light by silicon wafer, so the $J_{internal}$ and hence its related etching process have very small effect while ($J_{external}$) would sustain the etching process to become independent on the porous parameters and this could improve the etching at the early formed pits and pores. Etching will therefore continue in a fast rate at specific point where the density of the dangling bonds (nucleation sites) has a large population at these points.

Characterization of the Silver Nanoparticles/Porous Silicon Hybrid Structures

Surface Morphology of AgNPs/PS Hybrid Structures

The deposited AgNPs illustrate a multi-layer, continuous mud coating over the PS, resulting from homogeneous growth

Table 1 The obtained results of photoluminescence

Sample no.	Etching exposure time	PL wavelength (nm)	E_g (eV)	Nano-size (d) (nm)	PL intensity (au)
Sample 1 (LIE)	0	701	1.77	6.45	1099
Sample 2	5	682	1.82	6.29	1410
Sample 3	10	620	1.99	5.56	1625
Sample 4	15	591	2.1	5.24	2170
Sample 5	20	579	2.14	5.13	2450

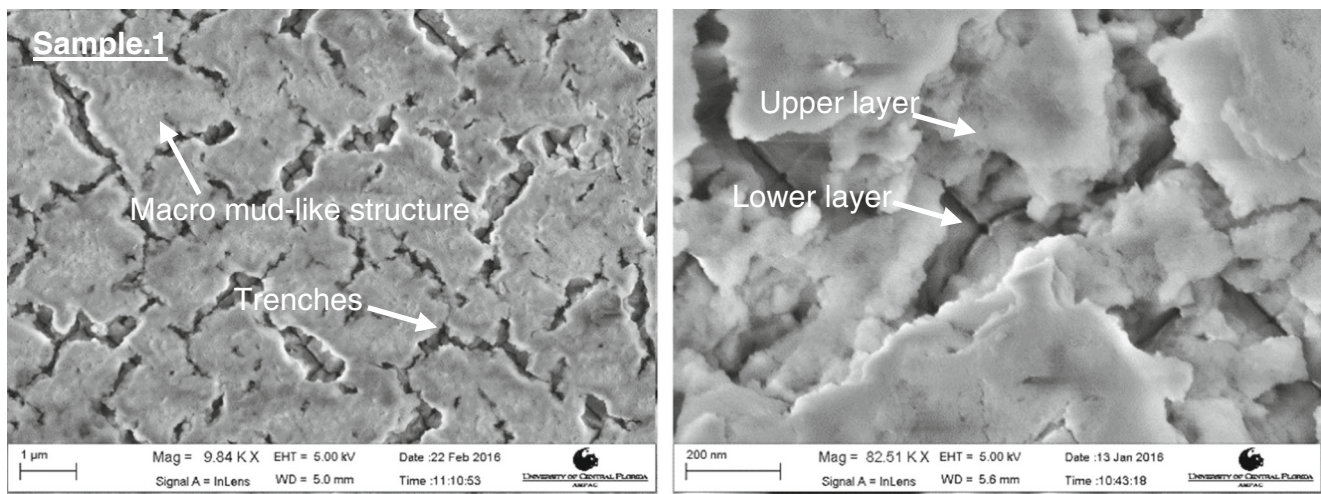


Fig. 6 FE-SEM image of AgNPs/PS hybrid structure and its magnification of sample 1

inside each mud, as shown in Fig. 6, where the mud regions are separated by trenches extended perpendicular over the layers. These observations refer to ion reduction process over silicon-rich with high density of pits and (Si–H₁) bonds. The presence of a second layer of nanoparticles over the primary one indicates a growth dependence on Weber-Vomer mechanism, in which the first layer is not fully covering the PS surface [25]. In other way, a second layer appeared because the density of surface nucleation sites Si–H₁ bonds is not fully occupied. In the primary layer, the trenches' sizes (regions

without silver nanoparticles) are smaller than those in the second layer, indicating a complete consumption of some Si–H₁ bonds during the growth process.

The resulting morphology of AgNPs with double etching mechanism is illustrated in Figs. 7, 8, 9, and 10, with features nearly dominated by large sizes (28–140 nm) of rod-like AgNP aggregations at a 63-nm peak.

The main AgNP layer features include the following: over PS surface growth, low nucleation density sites, and nano-rode configuration. The resulting nano-gaps are in the range

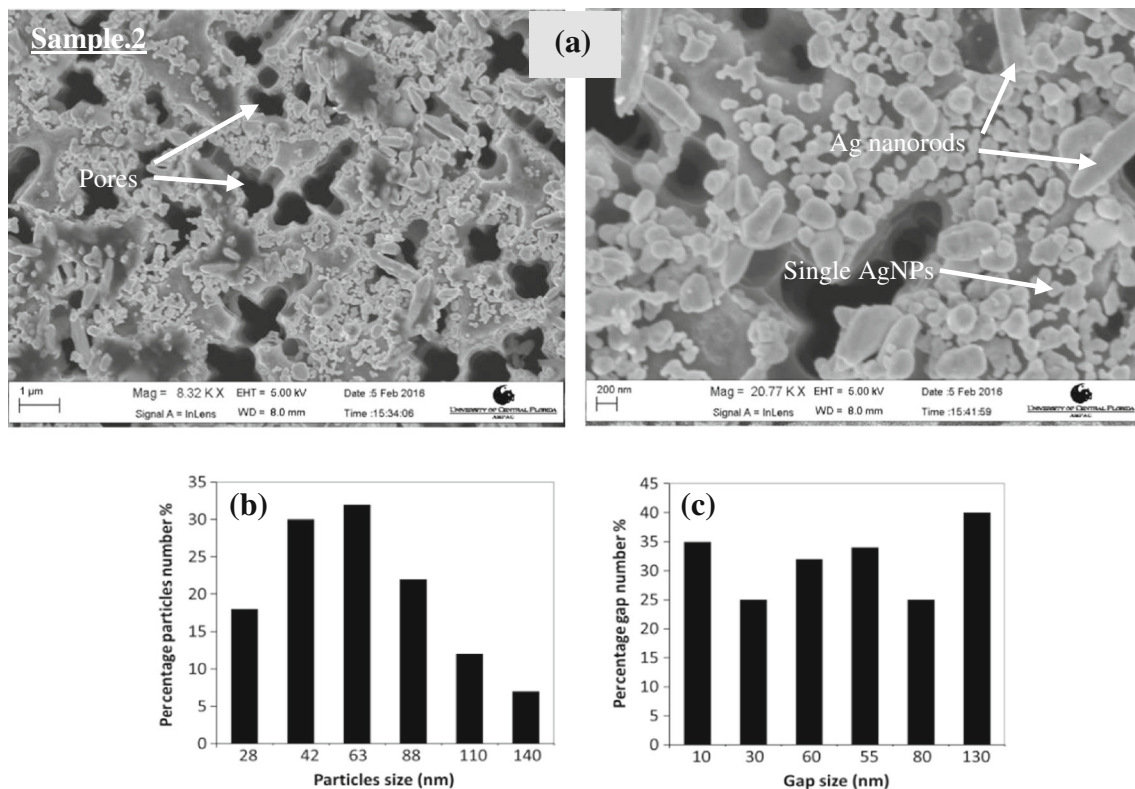


Fig. 7 a FE-SEM image of AgNPs/PS hybrid structure and its magnification, and the statistical distribution of b AgNP sizes and c nano-gap sizes of sample 2

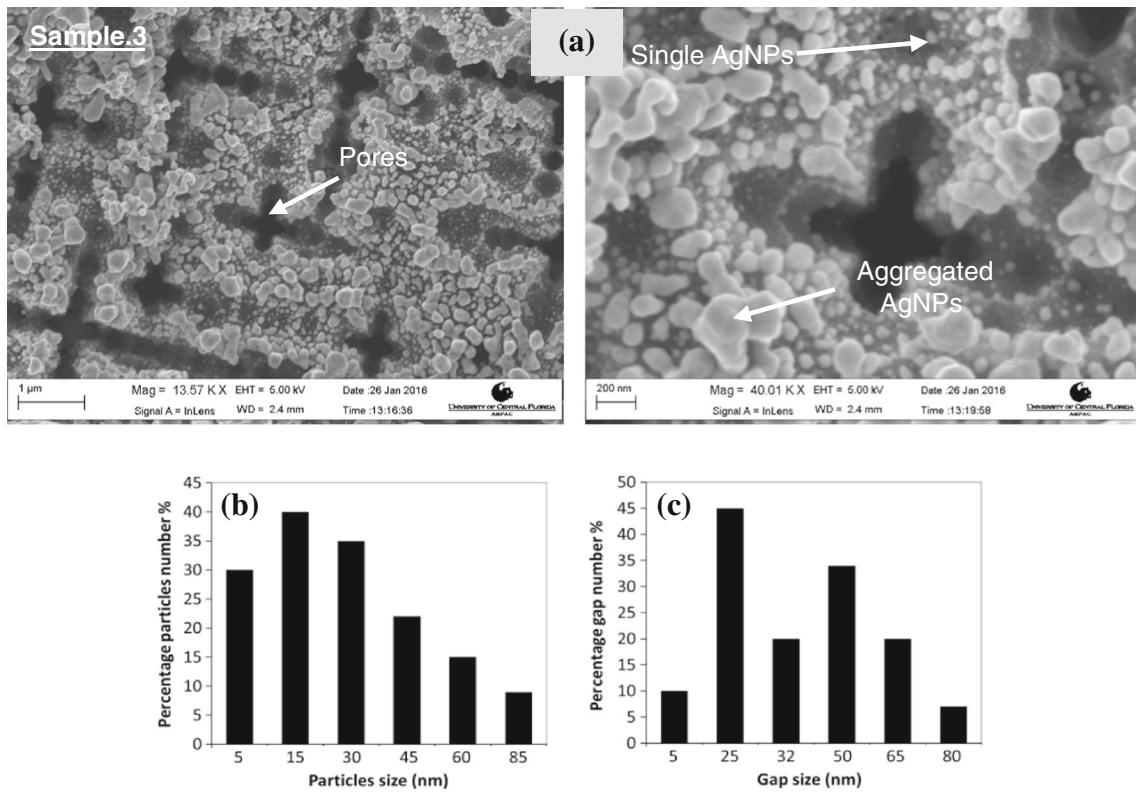


Fig. 8 a FE-SEM image of AgNPs/PS hybrid structure and its magnification, and the statistical distribution of **b** AgNP sizes and **c** nano-gap sizes of sample 3

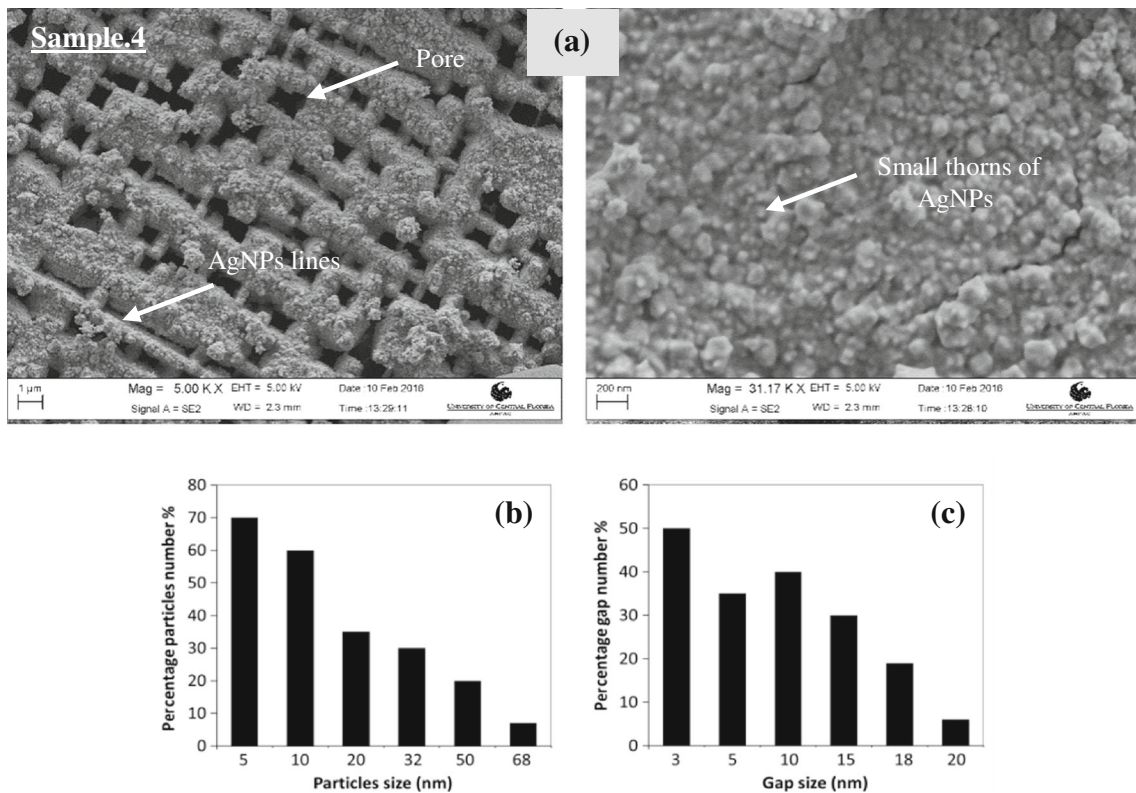


Fig. 9 a FE-SEM image of AgNPs/PS hybrid structure and its magnification, and the statistical distribution of **b** AgNP sizes and **c** nano-gap sizes of sample 4

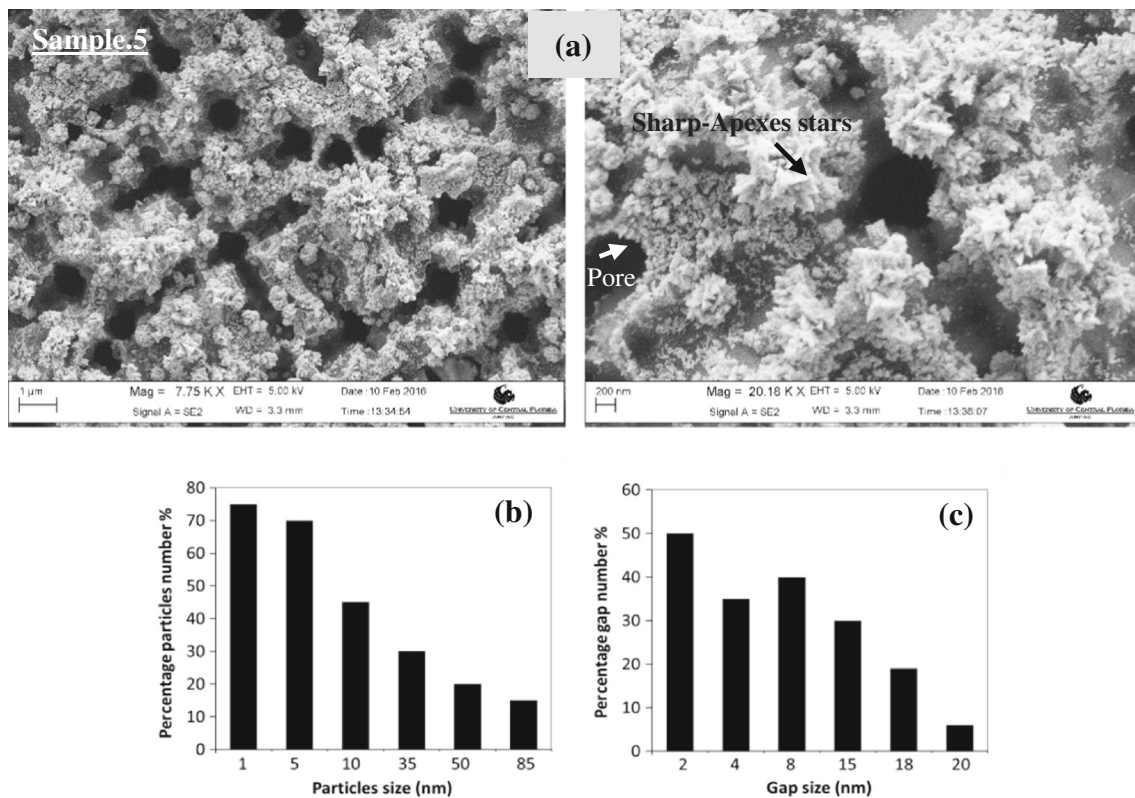


Fig. 10 a FE-SEM image of AgNPs/PS hybrid structure and its magnification, and the statistical distribution of **b** AgNP sizes and **c** nano-gap sizes of sample 5

of 10–130 nm with the highest peak at the greatest size, 130 nm. These resulting gaps are combinations of hot and cold nano-gaps, with cold nano-gaps greater than the hot ones, leading to weak Raman signal intensity improvement [26, 27]. Increasing the etching time to 10 min (sample 3) has enhanced the nucleation sites and modified the topography to have lower dimerization, and this made the AgNPs to assemble in smaller sizes which is comparable to sample 2. The silver nanoparticle sizes are in the range of 5–85 nm with peak distribution located at 15 nm.

The AgNP layer characterizations demonstrated rectangular structure, in which the AgNPs filling the pores with nano-gap density in the resulting nanoparticles to be within the range 5–80 nm and peak distribution located at 25 nm. The densities of cold and hotspot regions are comparable, yielding

a plasmonic contribution shared between the LSP and hotspot regions.

Further increase of exposure time to 15 min (sample 4) in PECE has reconstructed nanoparticle layer near the fiber mat layer. The nucleation sites showed very low, with nanoparticle size distribution ranging from 5 to 85 nm and a peak located at 5 nm.

The characterizations of this layer consist of isolated nanoparticle groups, increasing the tendency of the groups of nanoparticles on the upper surface to reconstruct themselves like carpet lines to completely cover the surface, and beginning growth of small thorn shapes. The resulting nano-gaps among the nanoparticles are ranging from 3 to 20 nm. Based on these values, this gap is just a hot gap so we can expect that the Raman intensity has a high value compared with the other

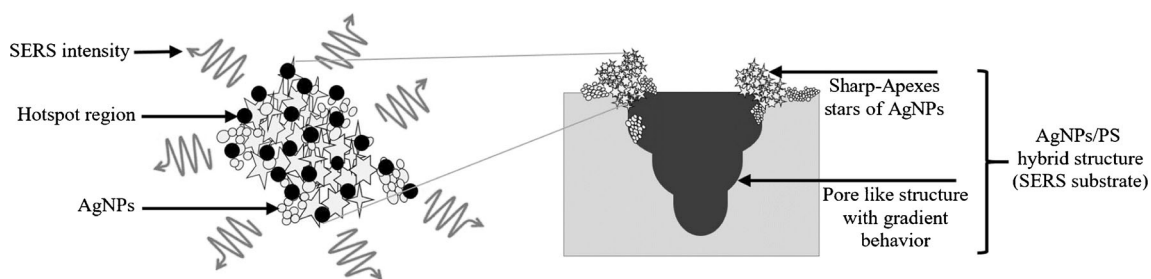
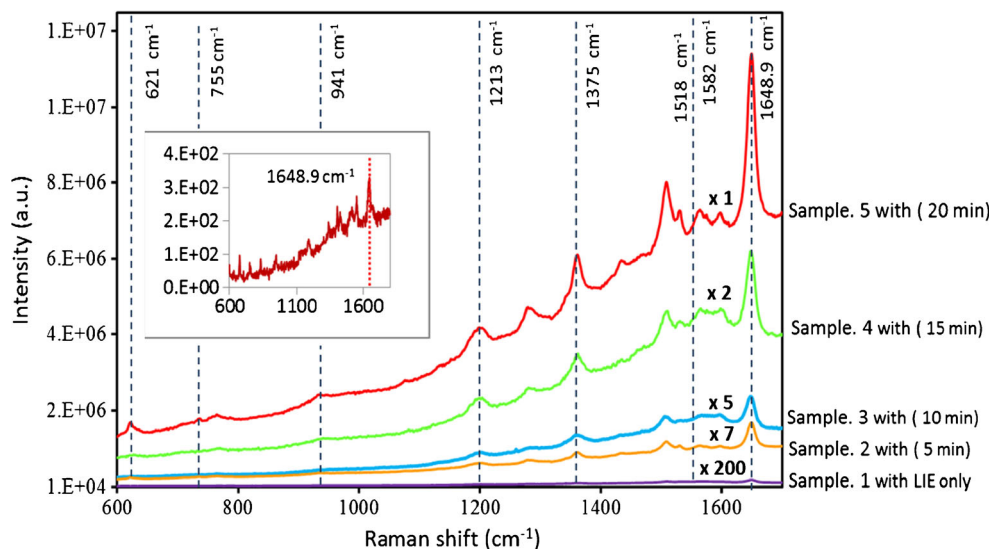


Fig. 11 Schematic illustration of the SERS improvement and hotspot regions which generated on the areas of *sharp-apexes stars* of AgNPs/PS hybrid structure (sample 5)

Fig. 12 SERS spectra from AgNPs/PSi hybrid structures (sample 1, sample 2, sample 3, sample 4, and sample 5) with concentration 10–15 M of the R6G molecule



samples. The increase of etching time to 20 min (sample 5) would change the overall morphology of the AgNP sizes to very small (minimum values) ranging from 1 to 85 nm and the surface of this layer is characterized with excessive broking process to fine structure nanoparticles to be as thorn stars,

irregular surface with sharp edges, and the growth extends to the pore sides.

The resulting nano-gaps have minimum values (2–20 nm) with a peak at about 2 nm. This very small size of nano-gaps can improve, to a very large extent, the resulting Raman

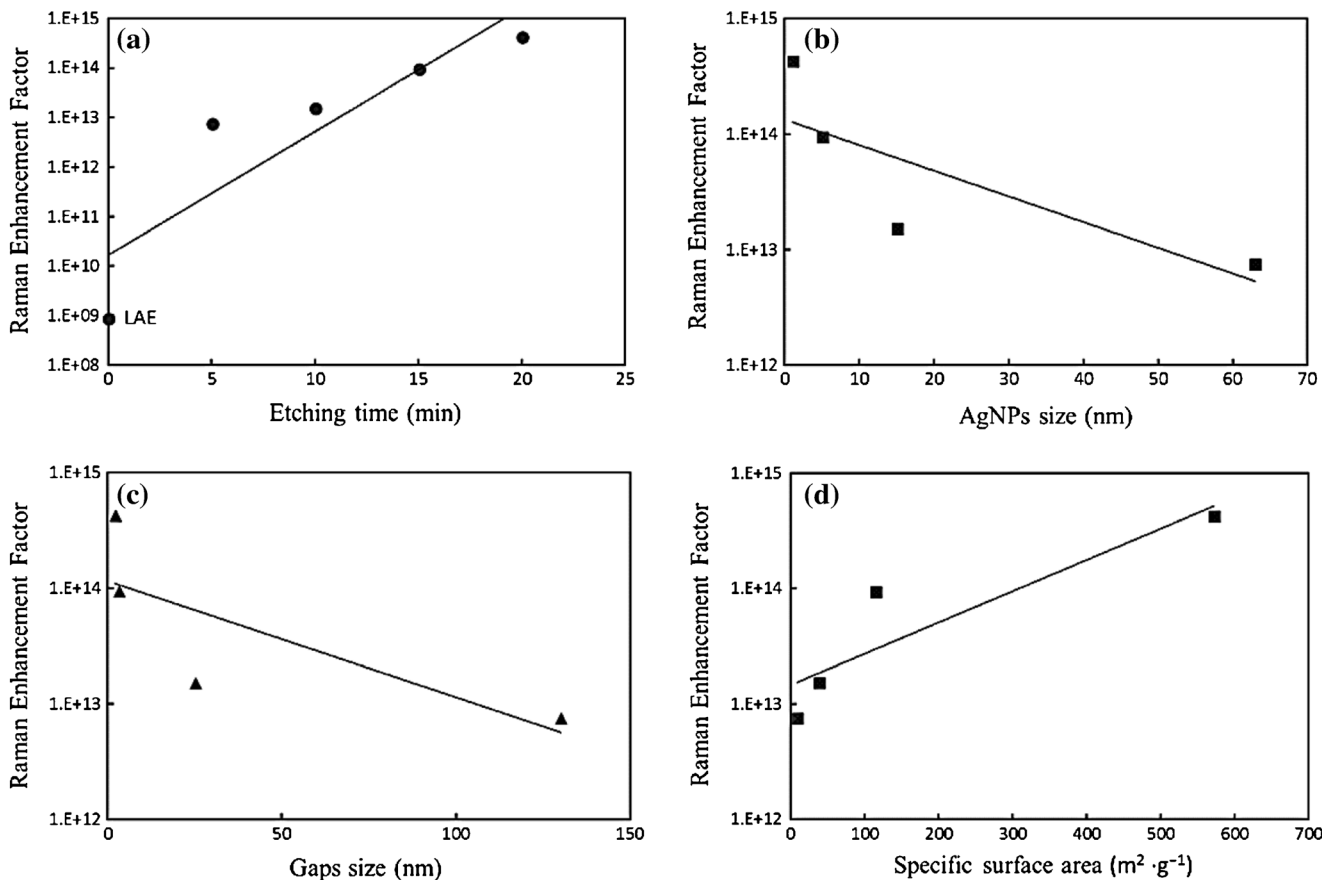
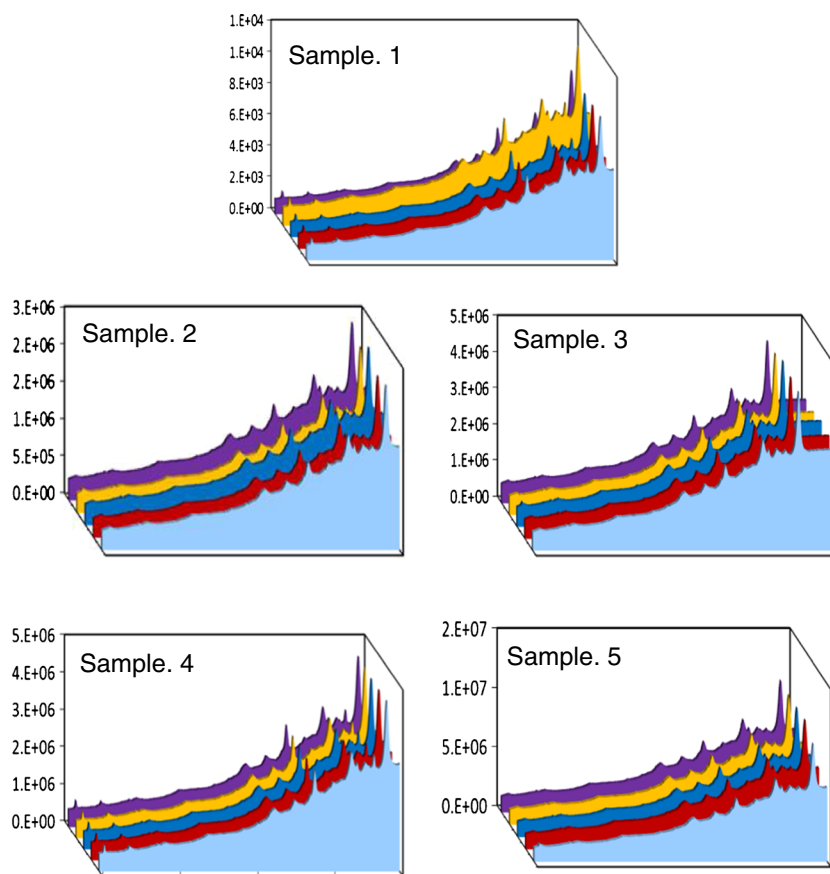


Fig. 13 Raman analytical enhancement factor as a function of **a** etching time, **b** AgNP size, **c** gap size, and **d** specific surface area of AgNPs (for samples 1, 2, 3, and 4)

Fig. 14 The reproducibility of SERS signal of R6G with sample 1, sample 2, sample 3, sample 4, and sample 5



spectra due to the formation of efficient hot gaps. The role of the hotspot regions of the R6G molecules on the PS surface of graded pore shapes is presented in Fig. 11. This figure can be considered as a suggested schematic of AgNPs/PS hybrid structure.

SERS Studies of AgNPs/PS Hybrid Structures

The SERS enhancement of the AgNPs/PS hybrid structures strongly relies on the isolated silver nanoparticle sizes, geometry, and the density of the hotspot regions (nanometer-sized gaps and nanometer-sized pits). The enhancement mechanism occurs in a two-step process. The first one is related to the local electromagnetic field enhancement, originating from the isolated plasmonic nanoparticles which acts as an optical antenna, and the second enhancement process establishes from the energy transfer of the (dye molecule/silver nanoparticles) under test system.

Figure 12 shows the Raman spectrum of the two types of PS structures prepared by LIE alone, and LIE followed by PECE. For sample 1, a very weak signal was observed in the spectra of 10^{-15} M of R6G located at 1648.9 cm^{-1} , while a number of distinguishable peaks were seen in the other hybrid structures of samples 2, 3, 4, and 5 at specific wave numbers 1648.9 , 1582 , 1518 , and 1375 cm^{-1} . These bonds

can be assigned to C–C bond stretching and C–H bond stretching which represent the finger print of the R6G molecule.

The analytical enhancement factor AEF is described by the ratio of target molecular concentrations as depicted in Eq. 12 [28]:

$$\text{AEF} = \frac{I_{\text{SERS}}/C_{\text{SERS}}}{I_{\text{RS}}/C_{\text{RS}}} \quad (12)$$

where I_{RS} is the Raman intensity, I_{SERS} is the SERS intensity, and C_{SERS} is the analyte in solution at a known concentration which is usually much smaller than C_{RS} (high concentration of target solution). This factor is appropriate to show how the surface enhancement increases the analytical ability of the Raman technique which depends on the structures of substrate and its coverage by the adsorbate. AEF values ranged between 8.64×10^8 and 7.15×10^{14} . Comparing the interesting peak of SERS spectra before and after depositing the AgNPs, the AEF was calculated and is plotted in Fig. 13a which represents the period of PECE dependence of the AEF. It can be seen that sample 5 has the highest AEF (7.15×10^{14}) while the lowest AEF (8.64×10^8) was obtained for the sample with LIE process alone. The variation in AEF values is very sensitive to the morphology of the deposited AgNPs. The LIE sample of the

fractal nano-structural regions has very small contribution in the Raman intensity improvement, i.e., facilitating a minimum AEF value, due to the absence of active hotspot regions and the presence of ineffective large-sized nanoparticle regions.

The SERS time dependence of the PECE process on the enhancement factor is strongly related to the density of the hotspots and the isolated AgNPs. The statistical distribution of the related plasmonic parameters (hotspots and plasmonic isolated nanoparticles) is illustrated in Fig. 13b, c. The maximum AEF was obtained for sample 5 which has high density of small-sized hotspots of about 2 nm, as shown in Fig. 10, and high density of isolated nanoparticles located at 1 nm size. The dependency of Raman AEF on both AgNP sizes and the related nano-gaps is illustrated in Fig. 13b, c. Figure 13d shows the relation between Raman AEF and the specific surface area of AgNPs. This figure demonstrates that the shape of nanoparticles has a significant role in AEF by improving the specific surface area. Increasing this area can improve, to a large extent, the effect of NPs in Raman signal. This is due to the high exposure area of nanoparticles and hence the effective energy transfer inside the hotspot regions. The specific surface area (surface area per mass) is one of the figures of the merits of the material and is given as:

$$\text{Specific surface area} = 6000 / D_p \times \rho \quad (13)$$

where D_p is the size of the AgNPs and ρ is the density of silver 10.5 g/cm^3 [29, 30].

To investigate the reproducibility of the fabricated samples, these SERS spectra were measured for different five batches of each sample. Figure 14 illustrates the intensity distribution of samples 1, 2, 3, 4, and 5 for R6G dye solution concentration 10^{-15} M .

The variation in Raman intensity of the main Raman peak 1648.9 cm^{-1} is illustrated in Fig. 15. Very poor reproducibility was recorded for sample 1. For samples 2, 3, 4, and 5, the reproducibility has improved as compared to that of sample 1. Maximum improvement (minimum variations of 5%) was obtained for sample 4. The main reason behind this performance depends on the uniformity of the surface morphology (macro specific uniformity) and the deposited silver nanoparticles, in addition to the size distribution of silver nanoparticles on the porous surface (micro specific uniformity).

Low variation (high reproducibility effect) means that both microscopic and macroscopic specific variations have a minimum value, while a higher variation of SERS spectrum to about 11% (poor reproducibility effect) reflects low microscopic and macroscopic uniformity.

The explanation of the above statement is supported by the measured surface morphology of the AgNPs/PS hybrid

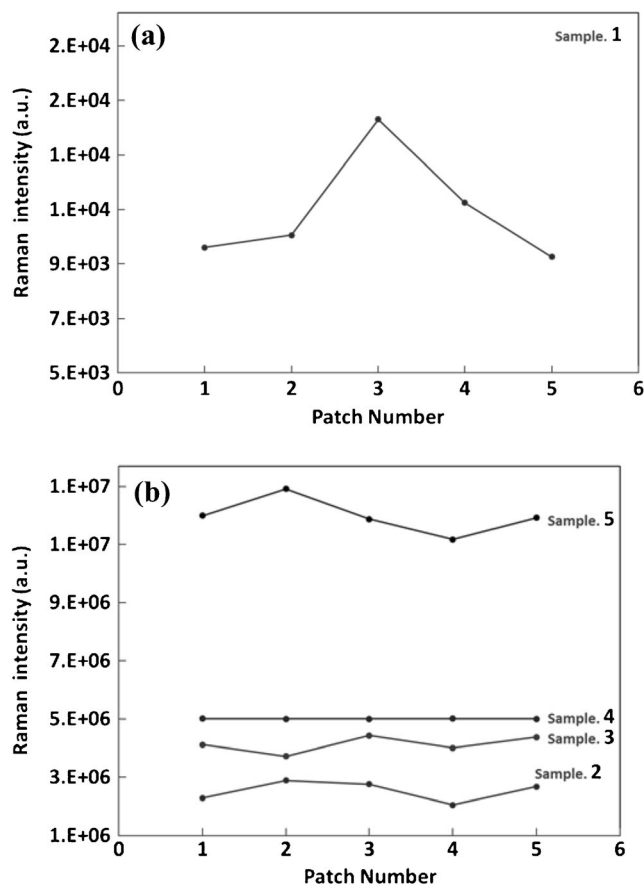


Fig. 15 The reproducibility of SERS signal of the main Raman peak 1648.9 cm^{-1} of 10^{-15} M of R6G of **a** sample 1, **b** sample 2, sample 3, sample 4, and sample 5

structure, where the highest reproducibility was achieved when the surface has minimum variation regions (3–20 nm), while the lowest reproducibility involves a surface variation region (10–130 nm).

Conclusion

In this work, a simple and efficient approach of double etching process was developed to fabricate SERS substrates with excellent reproducibility and high analytic enhancement factor for few molecule detection processes. Fine controlling of the PS morphologies led to form various types of plasmonic features. The SERS activity of various forms of plasmonic nanoparticles was evaluated for very low concentration 10^{-15} M of R6G dye (single molecule detection). The enhancement and reproducibility of SERS substrates improved with increasing of both efficient hotspots and specific surface area of AgNPs.

References

- Zhang D, Xiao SJ, Zheng LL, Lia YF, Huang CZ (2014) *Mater Chem B*
- Fleischmann M, Hendra PJ, McQuillan A (1974) Raman spectra of pyridine adsorbed at a silver electrode. *Chem Phys Lett* 26:163–166
- Li Q-l, Li B-w, Wang Y-q (2013) Surface-enhanced Raman scattering microfluidic sensor. *RSC Adv* 3:13015–13026
- Sánchez-Iglesias A, Aldeanueva-Potel P, Ni W, Pérez-Juste J, Pastoriza-Santos I, Alvarez-Puebla RA et al (2010) Chemical seeded growth of ag nanoparticle arrays and their application as reproducible SERS substrates. *Nano Today* 5:21–27
- Santos A, Kumeria T (2015) Electrochemical etching methods for producing porous silicon. In *Electrochemically engineered nanoporous materials*, ed. Springer, pp. 1–36
- Al-Khazraji KK, Rasheeda BG, Ibrahim MA, Mohammed AF (2012) Effect of laser-induced etching process on porous structures. *Procedia Eng* 38:1381–1390
- Soni R, Bassam G, Abbi S (2003) Laser-controlled photoluminescence characteristics of silicon nanocrystallites produced by laser-induced etching. *Appl Surf Sci* 214:151–160
- Yamanishi M, Suemune I (1983) Quantum mechanical size effect modulation light sources—a new field effect semiconductor laser or light emitting device. *Jpn J Appl Phys* 22:L22
- Kolasinski KW, Mills D, Nahidi M (2006) Laser assisted and wet chemical etching of silicon nanostructures. *J Vac Sci Technol Vacuums Surf Films* 24:1474
- Kowalik I, Guziejewicz E, Kopalko K, Yatsunenko S, Wójcik-Głodowska A, Godlewski M et al (2009) Structural and optical properties of low-temperature ZnO films grown by atomic layer deposition with diethylzinc and water precursors. *J Cryst Growth* 311:1096–1101
- Alwan AM, Hayder AJ, Jabbar AA (2015) Study on morphological and structural properties of silver plating on laser etched silicon. *Surf Coat Technol* 283:22–28
- Stewart MP, Buriak JM (2000) Chemical and biological applications of porous silicon technology. *Adv Mater* 12:859–869
- Menna P, Di Francia G, La Ferrara V (1995) Porous silicon in solar cells: a review and a description of its application as an AR coating. *Sol Energy Mater Sol Cells* 37:13–24
- Sun X, Wang N, Li H (2013) Deep etched porous Si decorated with au nanoparticles for surface-enhanced Raman spectroscopy (SERS). *Appl Surf Sci* 284:549–555
- Chan S, Kwon S, Koo TW, Lee LP, Berlin AA (2003) Surface-enhanced Raman scattering of small molecules from silver-coated silicon Nanopores. *Adv Mater* 15:1595–1598
- Panarin AY, Terekhov S, Kholostov K, Bondarenko V (2010) SERS-active substrates based on n-type porous silicon. *Appl Surf Sci* 256:6969–6976
- Adawiyah JH, Alwan MA, Allaa AJ (2016) Optimizing of porous silicon morphology for synthesis of silver nanoparticles. *Microporous Mesoporous Mater* 227:152–160
- Huang Z, Fang H, Zhu J (2007) Fabrication of silicon nanowire arrays with controlled diameter, length, and density. *Adv Mater* 19:744–748
- Tsuboi T, Sakka T, Ogata YH (1998) Metal deposition into a porous silicon layer by immersion plating: influence of halogen ions. *J Appl Phys* 83:4501–4506
- Antunez EE et al (2014) Controlled morphology and optical properties of n-type porous silicon: effect of magnetic field and electrode-assisted LEF. *Nanoscale Res Lett* 9.1:512
- Bisi O, Ossicini S, Pavese L (2000) Porous silicon: a quantum sponge structure for silicon based optoelectronics. *Surf Sci Rep* 38:1–126
- Sze SM (2008) *Semiconductor devices: physics and technology*: John Wiley & Sons
- Ben-Chorin M, Möller F, Koch F (1994) Nonlinear electrical transport in porous silicon. *Phys Rev B* 49:2981
- Peng C, Hirschman K, Fauchet P (1996) Carrier transport in porous silicon light-emitting devices. *J Appl Phys* 80:295–300
- Zheng H (2011) Molecular dynamic simulation of thin film growth stress evolution
- Novara C, Dalla Marta S, Virga A, Lamberti A, Angelini A, Chiadò A et al (2016) SERS-active ag nanoparticles on porous silicon and PDMS substrates: a comparative study of uniformity and Raman efficiency. *J Phys Chem C* 120:16946–16953
- Zhang C, Jiang SZ, Yang C, Li CH, Huo YY, Liu XY et al (2016) Gold@ silver bimetal nanoparticles/pyramidal silicon 3D substrate with high reproducibility for high-performance SERS. *Scientific reports*, vol. 6
- Le Ru E, Blackie E, Meyer M, Etchegoin PG (2007) Surface enhanced Raman scattering enhancement factors: a comprehensive study. *J Phys Chem C* 111:13794–13803
- Bykkam S, Ahmadipour M, Narisngam S, Kalagadda VR, Chidurala SC (2015) Extensive studies on X-ray diffraction of green synthesized silver nanoparticles. *Adv Nanopart* 4:1
- Harraz FA, Ismail AA, Bouzid H, Al-Sayari S, Al-Hajry A, Al-Assiri M (2015) Surface-enhanced Raman scattering (SERS)-active substrates from silver plated-porous silicon for detection of crystal violet. *Appl Surf Sci* 331:241–247